Efficient metallic spintronic emitters of ultrabroadband terahertz radiation

T. Seifert[1], S. Jaiswal[2,3], U. Martens[4], J. Hannegan[5], L. Braun[1], P. Maldonado[6], F. Freimuth[7], A. Kronenberg[2], J. Henrizi[2], I. Radu[8], E. Beaurepaire[9], Y. Mokrousov[7], P.M. Oppeneer[6], M. Jourdan[2], G. Jakob[2], D. Turchinovich[10], L.M. Hayden[5], M. Wolf[1], M. Münzenberg[4], M. Kläui[2], T. Kampfrath[1]

1. Department of Physical Chemistry, Fritz Haber Institute, 14195 Berlin, Germany
2. Institute of Physics, Johannes Gutenberg University, 55128 Mainz, Germany
3. Singulus Technologies AG, 63796 Kahl am Main, Germany
4. Institute of Physics, Ernst Moritz Arndt University, 17489 Greifswald, Germany
5. Department of Physics, University of Maryland Baltimore County, Baltimore, MD 21250
6. Department of Physics and Astronomy, Uppsala University, Uppsala, Sweden
7. Peter Grünberg Institute and Institute for Advanced Simulation, Forschungszentrum Jülich and JARA, Jülich, Germany
8. Institute for Optics and Atomic Physics, Technical University Berlin and Helmholtz-Zentrum Berlin für Materialien und Energie, Berlin, Germany
9. Institut de Physique et Chimie des Matériaux de Strasbourg, France
10. Max Planck Institute for Polymer Research, 55128 Mainz, Germany

Terahertz electromagnetic radiation is extremely useful for numerous applications such as imaging and spectroscopy. Therefore, it is highly desirable to have an efficient table-top emitter covering the 1-to-30-THz window whilst being driven by a low-cost, low-power femtosecond laser oscillator. So far, all solid-state emitters solely exploit physics related to the electron charge and deliver emission spectra with substantial gaps. Here, we take advantage of the electron spin to realize a conceptually new terahertz source based on tailored fundamental spintronic/photonic phenomena in magnetic metal multilayers: a spin-dependent generalization of the photo-Dember effect, the inverse spin-Hall effect and a broadband Fabry-Pérot resonance. Guided by an analytical model, such spintronic route offers unique possibilities for systematic optimization. We find that a 5.8-nm-thick W/CoFeB/Pt trilayer generates ultrashort THz pulses fully covering the 1-to-30-THz range. Our novel source outperforms standard emitters such as ZnTe(110) crystals in terms of bandwidth, conversion efficiency, flexibility, scalability and cost.

Introduction

The terahertz (THz) window, loosely defined as the frequency range from 0.3 to 30 THz in the electromagnetic spectrum, is located between the realms of electronics and optics[1,2]. As this region coincides with many fundamental resonances of materials, THz radiation enables highly selective spectroscopic insights into all phases of matter with high temporal[3,4] and spatial[5,6,7,8] resolution. Consequently, numerous applications in basic research[3,4], imaging[5] and quality control[8] have emerged.

To fully exploit the potential of THz radiation, energy-efficient and low-cost sources of ultrashort THz pulses are required. Most broadband table-top emitters are driven by femtosecond laser pulses that generate the required THz charge current by appropriately mixing the various optical frequencies[9,10]. Sources made from solids usually consist of semiconducting or insulating structures with naturally or artificially broken inversion symmetry. When the incident photon energy is below the semiconductor band gap, optical rectification causes a charge displacement that follows the intensity envelope of the incident pump pulse[9,10,11,12,13,14,15,16,17]. For above-band-gap excitation, the response is dominated by a photocurrent[18,19,20,21,22,23] with a temporally step-like onset and, thus, generally smaller bandwidth than optical rectification[9]. Apart from rare exceptions[14], most semiconductors used are polar (such as ZnTe, GaP[1,2], GaSe[12,13], GaAs[21,22] or organic materials[15,16,17]) and strongly attenuate THz radiation around optical phonon resonances, thereby preventing emission in the so-called Reststrahlen band located between ~1 and 15 THz. Consequently, nonpolar materials should be used to achieve broadband, gap-free THz emission.

Indeed, the so far most promising sources covering the full range from 1 to 20 THz and above are photocurrents in transient gas plasmas[9,10,24,25,26,27,28]. The downside of this appealing approach is that the underlying ionization process usually requires amplified laser pulses with high threshold energies on the order of 0.1 mJ. Measurable THz waveforms can be obtained with pump-pulse energies down to ~1 μJ, which is, however, still 2 to 3 orders of magnitude larger than what low-cost femtosecond laser oscillators can provide.

Another promising material class for realizing THz sources are metals[29] because they exhibit a pump absorptivity largely independent of wavelength[30], short electron lifetimes of ~10 to 50 fs[31] (implying broadband photocurrents), a featureless THz refractive index[32] (favoring gap-free emission) and a large heat conductivity (for efficient removal of excess heat). In addition, metal thin-film stacks (heterostructures) are well established, simple and cheap to fabricate, and they can be scaled easily. Recent works have indeed demonstrated metal THz emitters[33,34] with an efficiency comparable to ZnTe crystals[35,36], but only in conjunction with amplified laser pulses. Also, the bandwidth did not exceed 3 THz. Consequently, the full potential of metal-based THz emitters is far from being realized, and the key issue remains: to develop efficient sources covering the range from 1 to 30 THz without gaps, whilst being driven by ~1 nJ laser pulses from a typical, high-repetition-rate femtosecond laser oscillator.

At this point, it is important to acknowledge that all previously demonstrated THz emitters have taken advantage exclusively of the charge but not the spin of the electron. On the other hand, very recent tremendous progress in the fields of spintronics[37,38,39,40] and femtomagnetism[41] has shown that the electron spin offers entirely new possibilities to generate, steer and optimize transient currents in metals. In fact, spin-to-charge conversion has been revealed lately as a new mechanism for the generation of ultrafast photocurrents[42,43]. Unfortunately, even though fed by a millijoule-class laser, the resulting THz fields were much too weak for practical applications[42]. It remains to be shown whether the spintronic route can lead to a competitive THz emitter.

In this work, we exploit the unique spintronic and photonic properties of ultrathin metal films to realize a laser-oscillator-driven THz emitter that combines the benefits of existing emitters in one device: large bandwidth, high conversion efficiency, easy operation, scalability and low cost. This achievement results because our widely tunable approach provides access to a large set of spintronic metals and geometrical parameters for optimization.

Spintronic THz emitter

Figure 1a illustrates the basic principle of our spintronic THz emitter by means of a bilayer structure consisting of a ferromagnetic (FM) and nonferromagnetic (NM) metal thin film[42]. The FM layer is magnetized antiparallel to the *y*-axis. An incident femtosecond laser pulse excites electrons in the metals from states below the Fermi energy to states above. This transition changes the band velocity and lifetime of the electrons, such that they start moving. Since FM and NM layers have different transport properties, a net current along the *z*-axis is launched. In addition, because the product of density, band velocity and lifetime of spin-up (majority) electrons in FM metals (such as Fe, Co and Ni) is significantly higher than that of the spin-down (minority) electrons[31,44], the superdiffusive *z*-current is strongly spin-polarized[41]. This mechanism can be considered a spin-dependent generalization of the photo-Dember effect in semiconductors which arises from the different mobility of the photoinduced electrons and holes[19].

Once the spin current enters the NM layer, spin-orbit interaction deflects spin-up and spin-down electrons in opposite directions[37,38,39,40] (**Fig. 1a**). This inverse spin-Hall effect (ISHE) converts the longitudinal (*z*-directed) spin current density j_s into an ultrafast transverse (*x*-directed) charge current density $j_c = \gamma j_s$ and, thus, into THz radiation. Here, j_s and j_c are measured in units of electrons per area and time, and γ is the spin-Hall angle that can be understood as the mean deflection angle of a moving electron. Importantly, γ can have opposite sign in different metals such that engineering of spin-Hall currents becomes possible.

In our experiment, femtosecond pulses from a Ti:sapphire laser oscillator (duration 10 fs, center wavelength 800 nm, repetition rate 80 MHz) are used to both excite the THz emitters (with a pulse energy of only ~2.5 nJ) and to measure the transient THz electric field by electrooptic sampling[1,2,45] in suitable crystals and polymer films (see Methods). We start with bilayers consisting of FM $Co_{20}Fe_{60}B_{20}$ (thickness of 3 nm) capped by either NM Ta or Ir (3 nm). Typical THz electrooptic signals $S(t)$ obtained from these samples are displayed in **Fig. 1b**. Consistent with the generation mechanism outlined above[42], the emitted radiation has the following properties (see Supplementary Section S2): it is linearly polarized with the electric-field direction perpendicular to the sample magnetization. The spin current and, thus, THz field are reversed entirely, either when the external saturating magnetic field of 10 mT is reversed or when the two metallic films are grown in reverse

order on the substrate. The THz signal is independent of the pump polarization, and its amplitude grows linearly with the pump power (inset of **Fig. 1b**). This observation is very different from plasma sources which require a threshold pump intensity to obtain emission[24,25,26].

Fourier-transforming the time-domain signals $S(t)$ yields the spectral amplitude $|S(\omega)|$ vs frequency $\omega/2\pi$. A typical example is shown in **Fig. 1c**. Note this spectrum covers the large bandwidth from about 1 to 18 THz. We emphasize that spectral features such as the dip at 8 THz arise from the 50 µm thick GaP electrooptic sensor and not from the emitter[45]. By deconvoluting the detector transfer function from the signal $S(t)$, we obtain the THz electric field directly in front of the sensor (see Methods). Strikingly, the field amplitude spectrum (**Fig. 1c**) is remarkably smooth and extends from 1 to ≈30 THz full width at 10% amplitude maximum, without any gaps. In addition, the spectral phase of the transient field is flat (**Fig. 1c**), thereby demonstrating that the THz pulse is Fourier-limited. As discussed above, these features derive from the unique properties of metals: short-lived photocurrents and a featureless frequency dependence of the optical constants, in stark contrast to semiconductor THz emitters[9].

While its bandwidth is already impressive, the $Co_{20}Fe_{60}B_{20}$/Ta bilayer (**Fig. 1b**) generates a THz peak field about 2 orders of magnitude smaller than what is obtained from a 1 mm thick ZnTe(110) standard THz emitter under identical excitation conditions. To massively boost the THz amplitude, we need to understand the key factors that determine it. To this end, we derive the following relationship between the pump-induced spin current density j_s and the emitted x-polarized THz field E (**Fig. 1a**)

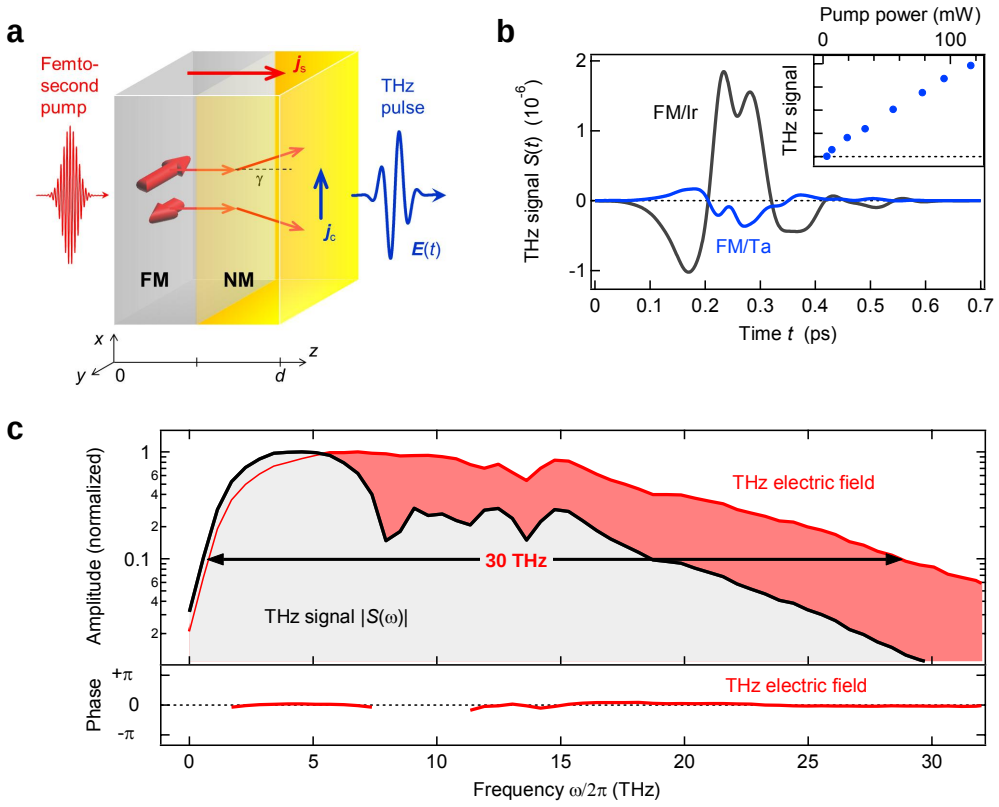

Figure 1 | Metallic spintronic THz emitter. a, Principle of operation. A femtosecond laser pulse excites electrons in the metal stack, thereby changing their band velocity and launching a current along the z-direction. Since the mobility of spin-up (majority) electrons is significantly higher than that of spin-down (minority) electrons, the z-current is spin-polarized. In the NM layer, spin-orbit interaction deflects spin-up and spin-down electrons in opposite directions and transforms the spin current j_s into an ultrafast transverse charge current j_c, leading to the emission of a THz electromagnetic transient. **b**, Electrooptic signal $S(t)$ of THz pulses obtained from photoexcited Ta- and Ir-capped $Co_{20}Fe_{60}B_{20}$ thin films and detected by a 50 µm thick GaP crystal. Inset: THz signal amplitude as a function of the incident pump power. **c**, Fourier spectra of the THz signal $S(t)$ and the transient THz electric field directly before the sensor as obtained by deconvolution of the detector response function from typical raw data such as those of **b**. The double-arrow illustrates the ≈30 THz bandwidth of the emitter, and the flat spectral phase attests the THz pulse is Fourier-limited.

directly behind the multilayer (see Supplementary Section S3):

$$E(\omega) = Z(\omega) e \int_0^d \mathrm{d}z\, \gamma(z) j_s(z,\omega). \qquad (1)$$

This equation can be interpreted as a generalized Ohm's law because the emitted field equals the total charge current $-e\int \mathrm{d}z\, \gamma j_s$ times an impedance $Z(\omega)$ which quantifies how efficiently a current is converted into electromagnetic radiation. Here, $-e$ is the electron charge, and Z is determined by

$$\frac{1}{Z(\omega)} = \frac{n_1(\omega) + n_2(\omega)}{Z_0} + \int_0^d \mathrm{d}z\, \sigma(z,\omega), \qquad (2)$$

where Z_0=377 Ω is the vacuum impedance, n_1 and n_2 denote, respectively, the refractive indices of the film substrate and the air, d is the film thickness, and σ is the conductivity of the metals. Equation (2) accounts for the propagation of the THz radiation inside the sample (including all reflection echoes) and the irradiation into free space. From a quasistatic viewpoint, $1/Z$ can be interpreted as the effective conductance of a parallel connection of all metal layers ($\int \mathrm{d}z\, \sigma$) shunted by the two adjacent half-spaces $[(n_1+n_3)/Z_0]$.

Equations (1) and (2) readily show that maximizing Z, γ and j_s will lead to maximum THz output of the emitter for a given pump power. The numerous sample parameters that can be tuned in such an optimization are the FM/NM materials and the geometry of the heterostructure.

Maximizing the THz output

NM layer. We start with varying the NM material which primarily affects the emitted THz field through the magnitude and sign of the spin-Hall angle γ [see Eq. (1)]. Consequently, we in particular consider such metals for which large γ values have been reported[38]. Importantly, for all samples studied, we find emitted THz waveforms and spectra whose shape is very similar to those shown in **Figs. 1b** and **1c**. Therefore, it is sufficient to quantify the THz emission efficiency by the root mean square (RMS) of the THz signal $S(t)$ which is displayed in **Fig. 2a** as a function of the NM metal in $Co_{20}Fe_{60}B_{20}$(3 nm)/NM(3 nm) heterostructures.

Figure 2a clearly shows that the THz field amplitude and polarity depend drastically on the NM material chosen: for instance, Pt delivers a 1 order of magnitude larger amplitude than Ta and Ir. Interestingly, choosing W for the NM layer leads to a comparable magnitude as with Pd or Pt, but with opposite sign. This observation is consistent with previous works[38]. The sign change arises because γ is roughly proportional to the spin-orbital polarization of the electronic states around the Fermi energy[46], which is opposite for the half-filled d-shell in W and the almost full d-shell in Pt.

More generally, we find that the entire trend of THz amplitude vs NM material (**Fig. 2a**) is in good

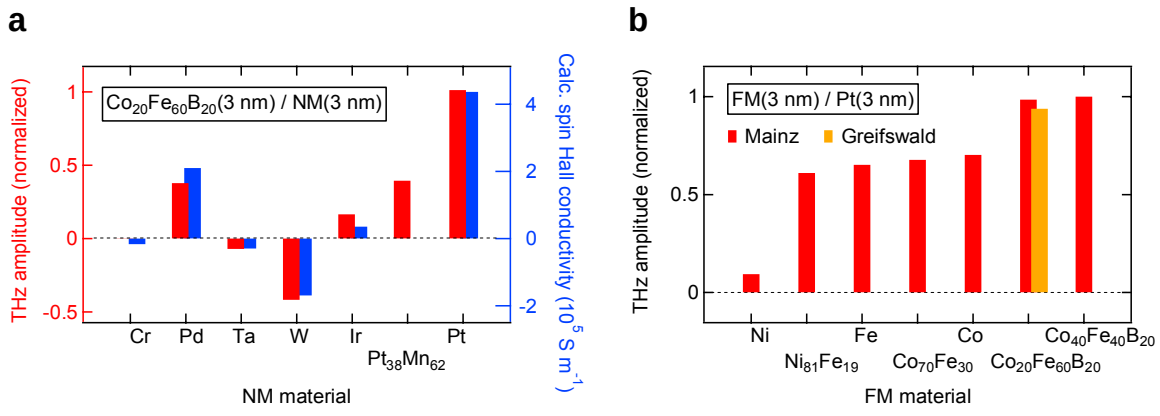

Figure 2 | Impact of material choice on emitter efficiency. a, Signal amplitude (RMS) of the emitted THz pulse as a function of the NM material used for the $Co_{20}Fe_{60}B_{20}$(3 nm)/NM(3 nm) stack (red bars). For comparison, *ab initio*-calculated values of the spin-Hall conductivity are also shown (blue bars), except $Pt_{38}Mn_{62}$. A Cr cap layer leads to nearly vanishing THz signal. **b**, THz amplitude of a FM(3 nm)/Pt(3 nm) heterostructure as a function of the FM material chosen. Different colors indicate different labs for sample fabrication (see Methods).

semiquantitative agreement with spin-Hall conductivities measured previously[38] and calculated by us (see **Fig. 2a** and Methods). This observation provides further evidence for the transport scenario outlined in **Fig. 1a** and Ref. 42. However, the major conclusion drawn from **Fig. 2a** is that Pt is the most promising NM material for our THz FM/NM bilayer emitter.

FM layer. In the second optimization step, we use Pt for the NM layer and study THz emission as a function of the FM material. We consider FM(3 nm)/Pt(3 nm) heterostructures with the FM metals Fe, Co, Ni and their binary alloys. Results are displayed in **Fig. 2b** and show that all materials provide similar efficiency, except Ni, which yields less than 20% of the maximum THz amplitude. The reason for this behavior is not yet understood but may be related to the fact that the Curie temperature of Ni (627 K) is considerably lower than that of all other FM materials (>1000 K). Note that adding B to Co-Fe alloys leads to an increase of the THz amplitude by about 30%. We attribute this behavior to the reduction of the FM conductivity by B impurities [see Eqs. (1) and (2)]. The essential conclusion is that $Co_{40}Fe_{40}B_{20}$/Pt heterostructures provide best THz-emission performance.

Sample thickness. In the third optimization step, we vary the stack geometry and first measure THz emission as a function of the total sample thickness d while keeping the FM and NM layer approximately equally thick. Our experimental data reveal a surprising behavior (**Fig. 3a**): the THz amplitude *increases* with *decreasing* emitter thickness d. This rise reaches a maximum at d=4 nm below which the THz amplitude falls off rapidly.

Such behavior is highly counterintuitive and in sharp contrast to most phase-matched frequency conversion schemes such as optical rectification or second-harmonic generation[9]. Indeed, Eq. (1) suggests that the THz amplitude scales with metal thickness d. Note, however, this trend is overcompensated by a remarkable photonic effect: our metal thin film acts as a Fabry-Pérot cavity that resonantly enhances both pump and THz waves. Because the cavity length d is much smaller than all wavelengths involved, all reflection echoes inside the film interfere constructively (**Fig. 3b**). The shorter the cavity, the more echoes occur before the wave has decayed, resulting in even more enhancement. Below a critical thickness d_c, however, reflection losses at the cavity faces exceed attenuation in the metal bulk. Then, the enhancement of pump and THz field saturates at $d<d_c$ and no longer compensates for the shrinking emitter volume. Therefore, the emitted THz amplitude should first grow with decreasing d and, after reaching a maximum, decrease, in agreement with our experimental bilayer data (**Fig. 3a**).

To model this behavior, we employ Eq. (1) in which the film impedance Z is obtained from Eq. (2) with the metal conductivities measured by THz transmission spectroscopy. The spin current density j_s is assumed to scale with the mean excitation density A/d. Here, A is the measured sample absorptance which amounts to as much as ~60%, nearly constant for d between 5 and 20 nm (see Supplementary

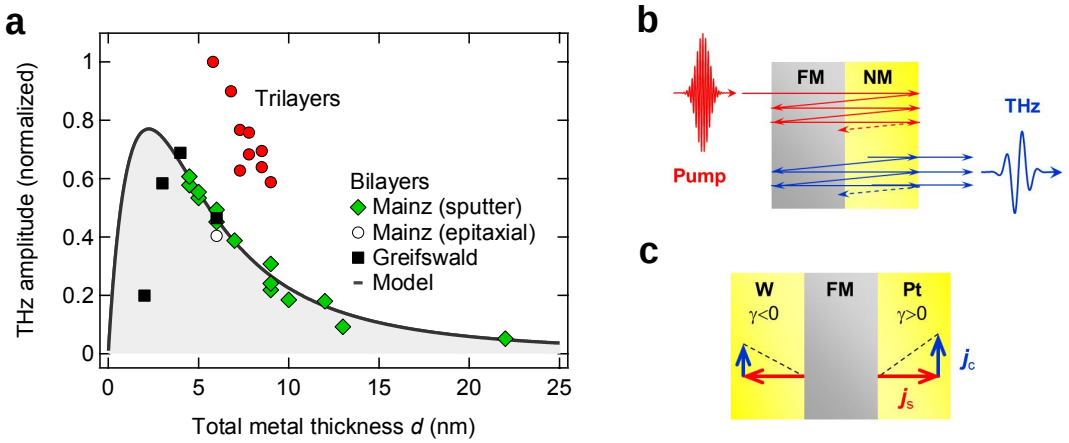

Figure 3 | Impact of stack geometry on emitter performance. a, THz amplitude (RMS) as a function of the thickness d of the metal stack. Different symbols represent different sample fabrication schemes (see Methods). The solid line is a fit using a transport model (see text). **b**, Schematic of the thin-film Fabry-Pérot cavity that enhances both incident pump and emitted THz radiation. **c**, Schematic of the trilayer emitter that converts the backward- and forward-propagating spin current j_s into a unidirectional charge current j_c with approximately equal efficiency.

Section S1). We note the thickness dependence of both Z and A/d exhibits the expected $1/(d+d_c)$-like behavior. To account for velocity randomization of the spin-current burst, we assume j_s decays exponentially[38] with a relaxation length λ_{rel} in the NM layer (see Supplementary Section S4).We fit our model to the THz amplitude data of **Fig. 3a** with λ_{rel} and a global amplitude factor being the only free parameters.

The best fit (solid curve in **Fig. 3a**) is obtained for λ_{rel}=1 nm and describes the thickness dependence of the emitted THz amplitude very well, including the existence of a maximum. The discrepancy for d<4 nm is most likely due to shortcomings of our simplified transport model and due to changes in the magnetic properties (such as Curie temperature) of the sample when approaching small thicknesses. In essence, **Fig. 3a** shows that the best THz emission efficiency is provided by the 4 nm thick $Co_{20}Fe_{60}B_{20}$/Pt emitter, and this performance is very close to the absolute maximum predicted by the model.

Trilayer. Having identified the best bilayer emitter, we finally engineer the sequence of the spintronic metal layers. **Figure 1a** suggests that only the forward-propagating half of the photoinduced spin current travels directly from the FM into the NM layer. The other, backward-flowing electrons need to undergo reflection at the substrate and longer propagation, resulting in current loss. This effect can be avoided by introducing another NM layer on the left-hand side of the FM film (**Fig. 3c**) which makes the structure more symmetric with respect to the spin current j_s but more asymmetric with respect to the charge current j_c. We choose W/$Co_{40}Fe_{40}B_{20}$/Pt because W and Pt exhibit the largest spin-Hall angles γ yet with opposite sign (**Fig. 2a**). Thanks to this unique possibility of spintronic engineering, the spin-Hall currents j_c in the W and Pt layer flow in the same direction, radiate in phase and, thus again, boost the THz amplitude (**Fig. 3c**).

Indeed, as seen in **Fig. 3a**, the THz amplitude from each W/$Co_{40}Fe_{40}B_{20}$/Pt trilayer is approximately twice as high as that from a bilayer counterpart with the same total thickness. In particular, the W(2 nm)/$Co_{40}Fe_{40}B_{20}$(1.8 nm)/Pt(2 nm) trilayer delivers a 40% higher THz amplitude than the best bilayer $Co_{20}Fe_{60}B_{20}$(2 nm)/Pt(2 nm), even though the trilayer is about 50% thicker. This result indicates that the conversion of both forward and backward spin currents into THz radiation overcompensates the larger metal thickness [see Eq. (1)].

These finding conclude our model-guided optimization strategy and identify the 5.8 nm thick W/$Co_{40}Fe_{40}B_{20}$/Pt trilayer as the best THz emitter out of the comprehensive set of more than 70 heterostructures studied here. With this extensive procedure, we have gone beyond all previous approaches for emitter design and fully exploited the spintronic nature of our THz source. The evolution of our efforts is illustrated by **Fig. 4a**: the trilayer delivers a more than 4 orders of magnitude larger THz power than $Co_{20}Fe_{60}B_{20}$(10 nm)/Ta(2 nm), which is one of the bilayers we started with.

Emitter performance test

To evaluate the performance of our spintronic emitter, we compare its output to that of the two standard THz sources employed to cover the range from about 0.3 to 8 THz: the nonlinear-optical crystals ZnTe(110) and GaP(110)[1,9]. To better identify spectral emission gaps, we choose a 70 µm thick Lemke/amorphous polycarbonate (LAPC) electrooptic sensor[14] that permits gap-free detection from about 0.3 to 15 THz. **Figure 4a** displays THz waveforms $S(t)$ from the three sources, measured under identical conditions. For ZnTe and GaP, the electrooptic signal $S(t)$ consists of a slow and fast oscillating part which are, respectively, related to frequencies below and above the Reststrahlen band of these crystals. In contrast, the signal from the spintronic trilayer features the highest peak amplitude, is much shorter (**Fig. 4a**) and even Fourier-limited (**Fig. 1c**).

As seen in **Fig. 4b**, emission spectra $|S(\omega)|$ from ZnTe and GaP suffer from considerable gaps from 3 to 10 THz and 7 to 13 THz, respectively, which coincide with the Reststrahlen bands of these materials[45]. We again emphasize that the spectrum of our emitter is, in contrast, gap-free and exceeds the spectral intensity of the ZnTe and GaP crystals over major frequency intervals, thereby outperforming these state-of-the-art emitters.

We use our spintronic trilayer emitter routinely to measure linear transmission spectra from 1 to 30 THz. As an example, **Fig. 4c** displays the amplitude and phase of the complex transmission of a 7.5 µm thick polytetrafluoroethylene (PTFE, Teflon®) sample, obtained by using the trilayer emitter

and a 10 µm thick ZnTe(110) sensor[45]. Resonant features around 6, 15 and 18 THz are found, and they arise, respectively, from CF_2 twisting, rocking/wagging and rocking in the molecular chain[47]. Our observation agrees excellently with previous PTFE studies using gas-plasma THz emitters[48], which, however, require 5 orders of magnitude higher pump-pulse energies. We finally note that such broadband and gapless THz spectroscopy would not be possible at all with standard solid-state emitters such as ZnTe or GaP crystals.

Conclusion

In conclusion, we have developed a conceptually new, efficient and versatile THz source based on optically driven spin currents in ultrathin magnetic metal heterostructures. Our approach unifies the benefits of different emitter types in one device: it approaches the bandwidth of much more expensive gas-plasma spectroscopy systems and delivers short, Fourier-limited pulses covering the full range from 1 to 30 THz without gap. As with often-used optical-rectification crystals, our heterostructure is robust, passive, easy-to-use (in transmission mode under normal incidence) and driven by a low-cost femtosecond laser oscillator. At the same time, the conversion efficiency of our emitter exceeds that of standard crystals such as ZnTe and GaP. Similar to biased photoconductive switches, direction and amplitude of the emitted THz field can easily be modulated by applying an oscillating magnetic field with small amplitude below 10 mT. In addition to these benefits, the broadband optical absorption of metals implies that the spintronic THz source can be driven by any oscillator, virtually independent of its output wavelength, for instance a Ti:sapphire (800 nm), Yb^{3+} fiber (1030 nm) or Er^{3+} fiber (1550 nm) laser.

We emphasize that fabrication of our emitter is inexpensive, straightforward and scalable, without invoking any lithography steps. Fabrication costs are dominated by the substrate price, and we are able to deposit homogeneous layers on substrates with diameters as large as 20 cm (see Methods). Driven by intense laser pulses, such large-area emitters exhibit a high potential for THz-field scaling, enabling nonlinear-optical studies[49,50] in the difficult-to-access region from 5 to 10 THz. Our results highlight metallic magnetic multilayers as a new and very promising class of efficient and broadband THz emitters. Finally, this work is an example for a rapid translation of recently discovered fundamental

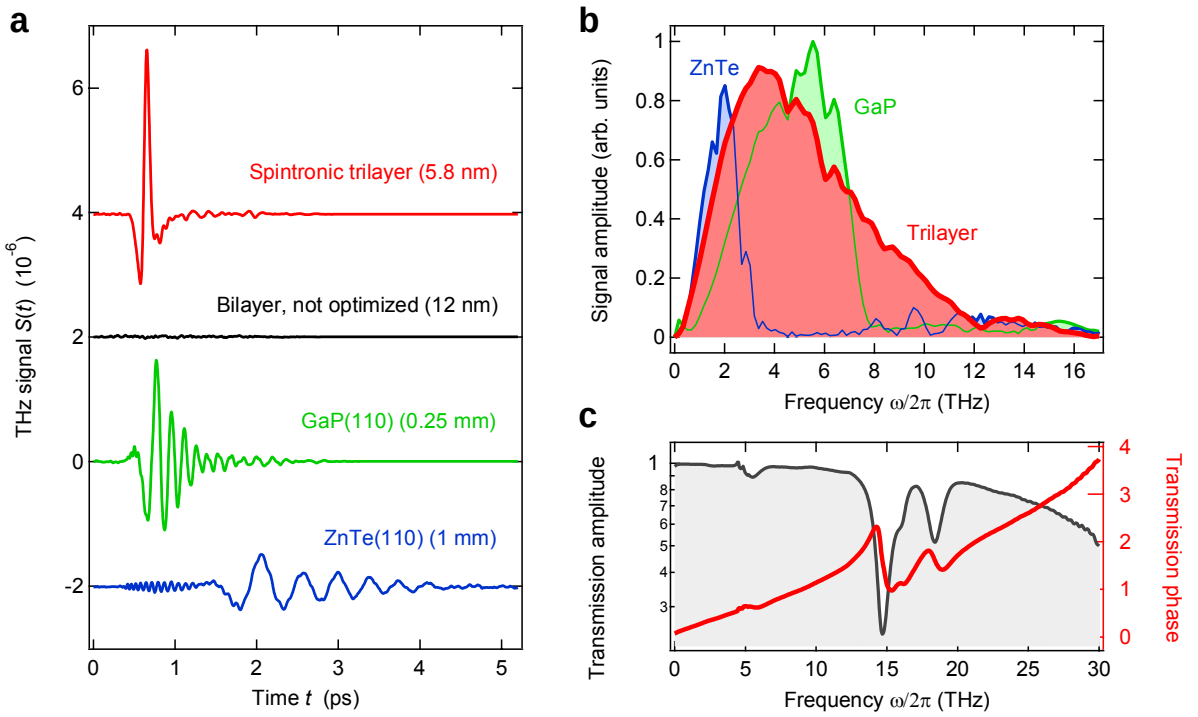

Figure 4 | Spintronic emitter performance and spectroscopic application. a, THz signal waveforms and **b**, resulting amplitude spectra of the spintronic trilayer emitter in comparison to standard THz emitters as measured with a 70 µm thick LAPC electrooptic sensor. Measurements are performed under identical conditions such that the output of the three emitters can directly be compared. **c**, Spectral amplitude and phase of the THz transmission of a 7.5 µm thick PTFE thread-seal tape conducted with our spintronic emitter and a 10 µm thick ZnTe sensor.

physical effects into useful technology that can straightforwardly be employed by the broad ultrafast-laser community.

Methods

Sample fabrication. The samples from the Mainz lab are deposited by Ar sputter deposition using a Singulus Rotaris deposition tool with targets of 100 mm diameter. The typical Ar pressure range is 2 to 4×10^{-3} mbar, and the power used is 800 W. Typical deposition rates are 1.2 Å s^{-1} for the FM layer and 2.1 Å s^{-1} for the NM layer. Prior to deposition, a short plasma etch is performed to clean the substrate surface from organic contaminants. The epitaxial Fe(100) thin film (thickness 3 nm) is prepared by RF-sputtering on a MgO(100) substrate at room temperature. After confirmation of the epitaxial growth by reflection high-energy electron diffraction (RHEED), an epitaxial Pt(100) layer (3 nm) is DC-sputtered on top. The $Co_{20}Fe_{60}B_{20}$ films from the Greifswald group are prepared by magnetron sputtering while NM metal films are grown by electron-beam evaporation under ultrahigh-vacuum conditions (base pressure 5×10^{-10} mbar) using *in situ* transfer. Composition analysis of the films yields a Co/Fe ratio of 1/2.1, and characterization by transmission-electron microscopy reveals smooth $Co_{20}Fe_{60}B_{20}$ film surfaces below the atomic-monolayer limit. The magnetic materials exhibit typical thin-film properties[51] and a nearly rectangular hysteresis curve with a coercive field below 10 mT. Substrate materials used are glass, sapphire and MgO.

Experimental details. In the optical experiment (**Fig. 1a**), the sample is kept in an external magnetic field of 10 mT and excited by linearly polarized laser pulses (duration 10 fs, center wavelength 800 nm, energy 2.5 nJ) from a Ti:sapphire laser oscillator (repetition rate 80 MHz) under normal incidence from the substrate side (beam diameter at sample 50 µm full width at half maximum of the intensity). The THz electric field is detected by electrooptic sampling[1,2,52] where probe pulses (0.6 nJ, 10 fs) from the same laser copropagate with the THz field through an electrooptic crystal. The resulting signal $S(t)$ equals twice the THz-field-induced probe ellipticity where t is the delay between the THz and probe pulse. To deconvolute the THz electric field incident on the sensor, we divide the Fourier-transformed signal $S(\omega)$ by the detector response function $H(\omega)$ and transform back into the time domain (see Supplementary Section S5). Depending on the signal strength and bandwidth required, we use various electrooptic materials: ZnTe(110) (thickness of 10 µm), GaP(110) (50 and 250 µm) and the poled polymer guest-host system Lemke/amorphous polycarbonate (LAPC)[14] (70 µm). All measurements are performed at room temperature in a N_2 atmosphere.

Theoretical model and calculations of spin-Hall angles. The spin-Hall conductivity (**Fig. 2a**) is calculated by means of the Kubo formula within density-functional theory using the full-potential linearized augmented plane-wave (FLAPW) program FLEUR (see http://www.flapw.de). We employ the generalized gradient approximation of the exchange correlation potential, a plane-wave cutoff at a wavevector of 85 nm^{-1} and the experimental lattice constants (2.91, 3.892, 3.302, 3.166, 3.8402 and 3.926 Å for Cr, Pd, Ta, W, Ir and Pt, respectively). Further details on the computation are given in Ref. 53.

References

[1] Ferguson, B. & Zhang, X. Materials for terahertz science and technology. *Nature Materials* 1, 26-33 (2002).

[2] Tonouchi, M. Cutting-edge terahertz technology. *Nature Photon.* 1, 97-105 (2007).

[3] Ulbricht, R., Hendry, E., Shan, J., Heinz, T. & Bonn, M. Carrier dynamics in semiconductors studied with time-resolved terahertz spectroscopy. *Rev. Mod. Phys.* 83, 543-586 (2011).

[4] Kampfrath, T., Tanaka, K. & Nelson, K. Resonant and nonresonant control over matter and light by intense terahertz transients. *Nature Photon.* 7, 680-690 (2013).

[5] Chan, W., Deibel, J. & Mittleman, D. Imaging with terahertz radiation. *Rep. Prog. Phys.* 70, 1325-1379 (2007).

[6] Cocker, T.L. et al. An ultrafast terahertz scanning tunnelling microscope. *Nature Photon.* 7, 620-625 (2013).

[7] Sano, Y. et al. Imaging molecular adsorption and desorption dynamics on graphene using terahertz emission spectroscopy. *Sci. Rep.* 4, 6046; DOI:10.1038/srep06046 (2014).

[8] Zeitler, J. et al. Terahertz pulsed spectroscopy and imaging in the pharmaceutical setting - a review. *Journal of Pharmacy and Pharmacology* 59, 209-223 (2007).

[9] Reimann, K. Table-top sources of ultrashort THz pulses. *Rep. Prog. Phys.* 70, 1597-1632 (2007).

[10] Blanchard, F. et al. Generation of Intense Terahertz Radiation via Optical Methods. *IEEE Journal of Selected Topics in Quantum Electronics* 17, 5-16 (2011).

[11] Rice, A. et al. Terahertz optical rectification from ⟨110⟩ zinc-blende crystals. *Appl. Phys. Lett.* 64, 1324 (1994).

[12] Kaindl, R., Eickemeyer, F., Woerner, M. & Elsaesser, T. Broadband phase-matched difference frequency mixing of femtosecond pulses in GaSe: Experiment and theory. *Appl. Phys. Lett.* 75, 1060 (1999).

[13] Huber, R., Brodschelm, A., Tauser, F. & Leitenstorfer, A. Generation and field-resolved detection of femtosecond electromagnetic pulses tunable up to 41 THz. *Appl. Phys. Lett.* 76, 3191 (2000).

[14] Zheng, X., Sinyukov, A. & Hayden, L.M. Broadband and gap-free response of a terahertz system based on a poled polymer emitter-sensor pair. *Appl. Phys. Lett.* 87, 081115 (2005).

[15] Zheng, X., McLaughlin, C.V., Cunningham, P., & Hayden, L.M. Organic broadband terahertz sources and sensors. *Journal of Nanoelectronics and Optoelectronics* 2, 58-76 (2007).

[16] Brunner, F. et al. A hydrogen-bonded organic nonlinear optical crystal for high-efficiency terahertz generation and detection. *Opt. Express* 16, 16496 (2008).

[17] Katayama, I., Akai, R., Bito, M., Shimosato, H., Miyamoto, K., Ito, H. & Ashida, M. Ultrabroadband terahertz generation using 4-N,N-dimethylamino-4'-N'-methyl-stilbazolium tosylate single crystals. *Appl. Phys. Lett.* 97, 021105 (2010).

[18] Shan, J., & Heinz, T.F. Terahertz radiation from semiconductors. In *Ultrafast Dynamical Processes in Semiconductors* (pp. 1-56). Springer Berlin Heidelberg. (2004).

[19] Apostolopoulos, V. & Barnes, M. THz emitters based on the photo-Dember effect. *Journal of Physics D: Applied Physics* 47, 374002 (2014).

[20] Klatt, G. et al. Terahertz emission from lateral photo-Dember currents. *Opt. Express* 18, 4939 (2010).

[21] Shen, Y., Upadhya, P., Linfield, E., Beere, H. & Davies, A. Ultrabroadband terahertz radiation from low-temperature-grown GaAs photoconductive emitters. *Appl. Phys. Lett.* 83, 3117 (2003).

[22] Hale, P. et al. 20 THz broadband generation using semi-insulating GaAs interdigitated photoconductive antennas. *Opt. Express* 22, 26358 (2014).

[23] Berry, C., Wang, N., Hashemi, M., Unlu, M. & Jarrahi, M. Significant performance enhancement in photoconductive terahertz optoelectronics by incorporating plasmonic contact electrodes. *Nature Communications* 4, 1622 (2013).

[24] Thomson, M.D., Kreß, M., Löffler, T. & Roskos, H.G. Broadband THz emission from gas plasmas induced by femtosecond optical pulses: From fundamentals to applications. *Laser & Photon. Rev.* 1, 349–368 (2007).

[25] Kim, K., Glownia, J., Taylor, A.J. & Rodriguez, G. High-Power Broadband Terahertz Generation via Two-Color Photoionization in Gases. *IEEE Journal of Quantum Electronics* 48, 797-805 (2012).
[26] Lu, X. & Zhang, X.C. Investigation of ultra-broadband terahertz time-domain spectroscopy with terahertz wave gas photonics. *Frontiers of Optoelectronics* 7, 121-155 (2013).
[27] Bartel, T., Gaal, P., Reimann, K., Woerner, M. & Elsaesser, T. Generation of single-cycle THz transients with high electric-field amplitudes. *Opt. Lett.* 30, 2805-2807 (2005).
[28] Buccheri, F. & Zhang, X.C. Terahertz emission from laser-induced microplasma in ambient air. *Optica* 2, 366 (2015).
[29] Ramanandan, G., Ramakrishnan, G., Kumar, N., Adam, A. & Planken, P. Emission of terahertz pulses from nanostructured metal surfaces. *Journal of Physics D: Applied Physics* 47, 374003 (2014).
[30] Zhang, L. et al. High-power THz to IR emission by femtosecond laser irradiation of random 2D metallic nanostructures. Sci. Rep. 5, 12536; doi: 10.1038/srep12536 (2015).
[31] Zhukov, V., Chulkov, E. & Echenique, P. Lifetimes and inelastic mean free path of low-energy excited electrons in Fe, Ni, Pt, and Au: Ab initio GW + T calculations. *Phys. Rev. B* 73, 125105 (2006).
[32] Laman, N. & Grischkowsky, D. Terahertz conductivity of thin metal films. *Appl. Phys. Lett.* 93, 051105 (2008).
[33] Ramakrishnan, G. & Planken, P. Percolation-enhanced generation of terahertz pulses by optical rectification on ultrathin gold films. *Optics Letters* 36, 2572 (2011).
[34] Polyushkin, D., Hendry, E., Stone, E. & Barnes, W. THz Generation from Plasmonic Nanoparticle Arrays. *Nano Letters* 11, 4718-4724 (2011).
[35] Kadlec, F., Kuzel, P. & Coutaz, J. Study of terahertz radiation generated by optical rectification on thin gold films. *Optics Letters* 30, 1402 (2005).
[36] Welsh, G.H., Hunt, N.T. & Wynne, K. Terahertz-Pulse Emission Through Laser Excitation of Surface Plasmons in a Metal Grating. *Phys. Rev. Lett.* 98, 026803 (2007).
[37] Saitoh, E., Ueda, M., Miyajima, H. & Tatara, G. Conversion of spin current into charge current at room temperature: Inverse spin-Hall effect. *Appl. Phys. Lett.* 88, 182509 (2006).
[38] Hoffmann, A. Spin Hall Effects in Metals. *IEEE Trans. Magn.* 49, 5172-5193 (2013).
[39] Sinova, J., Valenzuela, S.O., Wunderlich, J., Back, C.H. & Jungwirth, T. Spin Hall effects. *Rev. Mod. Phys.* (accepted), see http://journals.aps.org/rmp/accepted/58077E11Q8f15e01e0aa5510b2767e3da25148b87
[40] Wei, D. et al. Spin Hall voltages from a.c. and d.c. spin currents. Nat. Commun. 5:3768 doi: 10.1038/ncomms4768 (2014).
[41] Battiato, M., Carva, K. & Oppeneer, P.M. Superdiffusive spin transport as a mechanism of ultrafast demagnetization. *Phys. Rev. Lett.* 105, 027203 (2010).
[42] Kampfrath, T. et al. Terahertz spin current pulses controlled by magnetic heterostructures. *Nature Nanotech* 8, 256-260 (2013).
[43] Héroux, J.B., Ino, Y., Kuwata-Gonokami, M., Hashimoto, Y. & S. Katsumoto, S. Terahertz radiation emission from GaMnAs. Appl. Phys. Lett. 88, 221110 (2006).
[44] Jin, Z. et al. Accessing the fundamentals of magnetotransport in metals with terahertz probes. *Nat. Phys.* (2015). doi:10.1038/nphys3384
[45] Leitenstorfer, A., Hunsche, S., Shah, J., Nuss, M. & Knox, W. Detectors and sources for ultrabroadband electro-optic sampling: Experiment and theory. *Appl. Phys. Lett.* 74, 1516 (1999).
[46] Kontani, H., Tanaka, T., Hirashima, D., Yamada, K. & Inoue, J. Giant Orbital Hall Effect in Transition Metals: Origin of Large Spin and Anomalous Hall Effects. *Phys. Rev. Lett.* 102, (2009).
[47] Chantry, G. et al. The far infrared spectrum of crystalline polytetrafluoroethylene. *Polymer* 15, 69-73 (1974).
[48] D'Angelo, F., Mics, Z., Bonn, M. & Turchinovich, D. Ultra-broadband THz time-domain spectroscopy of common polymers using THz air photonics. *Opt. Express* 22, 12475 (2014).
[49] Liu, M. et al. Terahertz-field-induced insulator-to-metal transition in vanadium dioxide metamaterial. *Nature* 487, 345–348 (2012).

[50] Vicario, C. *et al*. Off-resonant magnetization dynamics phase-locked to an intense phase-stable terahertz transient. Nat. Photonics 7, 720–723 (2013).

--- Refs of Methods section ---

[51] Boulle, O., Malinowski, G. & Kläui, M. Current-induced domain wall motion in nanoscale ferromagnetic elements. *Materials Science and Engineering: R: Reports* 72, 159-187 (2011).

[52] Leitenstorfer, A., Hunsche, S., Shah, J., Nuss, M. & Knox, W. Detectors and sources for ultrabroadband electro-optic sampling: Experiment and theory. *Appl. Phys. Lett.* 74, 1516 (1999).

[53] Freimuth, F., Blügel, S. & Mokrousov, Y. Anisotropic spin Hall effect from first principles. *Phys. Rev. Lett.* 105, 246602 (2010).